PHYSICAL REVIEW B

CONDENSED MATTER

THIRD SERIES, VOLUME 49, NUMBER 8 15 FEBRUARY 1994-II

Experimental and theoretical determination of the electronic structure and optical properties of three phases of ZrO_2

R. H. French, S. J. Glass,* and F. S. Ohuchi†
DuPont Company, Central Research and Development, Experimental Station, Wilmington, Delaware 19880

Y. -N. Xu and W. Y. Ching
Department of Physics, University of Missouri–Kansas City, Kansas City, Missouri 64110-2499
(Received 4 October 1993)

The addition of suitable dopants to ZrO_2 can induce dramatic phase stabilization, and this dopant-induced phase stabilization is the basis of transformation toughening of zirconia-based structural ceramics. We have determined the electronic structure of three phases of ZrO_2, cubic, tetragonal, and monoclinic, using vacuum-ultraviolet and x-ray-photoemission spectroscopies, coupled with *ab initio* band-structure and optical property calculations using the orthogonalized linear-combination-of-atomic-orbitals method, in an attempt to understand the complex interaction of the stabilizing dopants and associated atomic defects with the crystal structures of ZrO_2 and their phase transitions. The experimental samples were single or polycrystalline stabilized materials which contain atomic defects, while the calculations were performed for undoped idealized ZrO_2 structures without atomic defects. Reasonable agreement is found between experiment and theory at this level. The primary difference among the three phases of ZrO_2 is the hybridization or mixing of the Zr 4*d* (x^2-y^2 and z^2) and the Zr 4*d* (*xy*, *yz*, and *zx*) bands, which form the conduction bands as the symmetry decreases from cubic to monoclinic. This leads to a complex evolution of the O 2*p* to Zr 4*d* and the O 2*s* to Zr 4*d* interband transitions. In addition, in the real materials, the presence of yttrium stabilizer introduces additional Y 4*p* valence bands and Y 4*d* conduction bands. The effective coordination of zirconium by oxygen is reduced from eightfold to sevenfold by the presence of the stabilizing ions and defects and this leads to the introduction of an occupied Zr 4*d* valence band suggestive of the presence of Zr^{2+}.

I. INTRODUCTION

There has been great technological and scientific interest in ZrO_2 for ceramic, optical, and thin-film applications, and it has also been the focus of first-principles studies of phase transitions and dopant-induced phase stabilization. At temperatures below 1170 °C, the monoclinic (*m*) phase of undoped ZrO_2 is thermodynamically stable. From 1170 to 2370 °C undoped ZrO_2 is tetragonal (*t*), while above 2370 °C undoped ZrO_2 is a cubic (*c*) material until the melt forms at 2706 °C.[1] The *c* phase can be dramatically stabilized (i.e., the *c* to *t* phase transformation temperature can be lowered to room temperature) by the addition of solutes such as MgO, CaO, Y_2O_3, etc. The addition of these solutes also allows the sintering of powder compacts to take place in single-phase fields of *c*- or *t*-ZrO_2 at reasonable temperatures. Both ZrO_2 phase transformations and stabilization have been the subject of wide scientific study including optical[2] and phonon[3] studies, band[4] and cluster-based[5–8] electronic-structure calculations, and free-energy calculations.[9] These studies provide the opportunity to identify and understand dopant-induced phase stabilization mechanisms that could be applicable to other systems.

The tetragonal-to-monoclinic phase transformation in zirconia has generated intense technological interest in zirconia and composites containing zirconia, because the phase transformation can be harnessed to toughen the material, thereby improving its mechanical properties.[10] The toughening arises because of the metastability of *t* precipitates in partially stabilized zirconias and of *t*-ZrO_2 in tetragonal zirconia polycrystals. When metastable *t*-ZrO_2 experiences localized tensile stresses during the propagation of a crack, it can transform to the *m* phase. Because the phase transformation is accompanied by a +4% volume strain ($\Delta V/V$), the transformation of the *t* particles in the vicinity of a propagating crack acts to reduce the stress intensity at the crack tip. Further details of this toughening mechanism can be found in the work of McMeeking and Evans.[11]

There is also interest in the electronic structure and defect chemistry of zirconia because it is an oxygen-ion conductor and, therefore, can be used in oxygen sensors,[12] oxygen pumps for partial pressure regulation,[13] and fuel cells for electricity generation.[14] The ionic conductivity of zirconia arises due to the large number of oxygen vacancies introduced when divalent (Mg^{2+}) or trivalent ions (Y^{3+}) are incorporated into the zirconia structure for the purpose of phase stabilization.

In this paper, we examine the optical properties of the three phases of ZrO_2 with vacuum-ultraviolet (VUV) and valence-band x-ray-photoemission spectroscopies (VB-XPS) combined with *ab initio* band-structure calculations. Combined experimental and theoretical studies in this system are complicated due to the issue of atomic defects and stabilizing dopants. The room-temperature experimental study of the *t* and *c* phases, which in their unstabilized and nondefective form are unstable at room temperature, requires the presence of appreciable concentrations of stabilizing dopants and associated oxygen vacancies in the samples. Theoretical band-structure calculations of the electronic structure to highlight the effects of crystal structure are presently limited to certain idealized room-temperature structures, such as band-structure calculations of undoped defect-free ZrO_2 phases, without vacancies or Y.[15] There have been detailed theoretical calculations of the electronic structure of small clusters of atoms containing the stabilizing dopants and atomic defects,[16] but these are typically in the higher symmetry cubic crystal structure, and even these cluster calculations have not yet presented the optical properties of ZrO_2 from first principles. The complex nature of the interaction of the defects and the crystal structures and the resulting stabilization of the phases can be seen in the experimental results presented here. The comparison of the real and idealized materials serves as a useful starting point for investigation. Another difficulty in the study of ZrO_2 is acquiring appropriate samples for optical studies. Transparent single crystals of stabilized *c*-ZrO_2 are high-quality optical materials, but contain the largest stabilizer additions. The stabilized *t* phase commonly exists only in the polycrystalline form, which is less than ideal for optical studies, while *m* single crystals, which require no stabilizer additions, exhibit extensive, phase-transformation-induced microtwinning.

II. METHODS

A. Sample preparation

The *m*- and *c*-ZrO_2 samples were supplied by Ceres Corporation.[17] The *c*-ZrO_2 specimens are transparent single crystals, stabilized with 9.5 mol % Y_2O_3 and grown by the method described in Ref. 18. The *m* sample was grown from an undoped ZrO_2 melt in the *c* phase and underwent the transformations from *c*- to *t*- to *m*-ZrO_2 upon cooling to room temperature. This produces a single-crystal *m* sample which is heavily microtwinned and appears white at room temperature due to light scattering. The polycrystalline *t* sample is stabilized in the *t* form with 4.5 mol % Y_2O_3. This specimen was pressed from a commercially available powder[19] and sintered at 1500 °C for 2 h.[20] Its density is greater than 99.5% of the theoretical density. The structural parameters of the *c* and *t* phases of ZrO_2, as determined from x-ray crystallography, are summarized in Table I, while for the *m* phase literature values are reported due to the difficulty of determining the lattice parameters of the microtwinned sample used in the present study. In the three ZrO_2 phases there are 4 ZrO_2 molecules per unit cell. The presence of Y_2O_3 stabilizer in *c*- or *t*-ZrO_2 has been found to increase the unit-cell parameters in a linear manner from 5.122 Å for 4.5 mol % Y_2O_3 to 5.138 Å for 9.5 mol % Y_2O_3 for the case of *c*-ZrO_2,[21] which is comparable to the variations found in this study for the *t*- and *c*-ZrO_2 samples. The transformation from the *t* to the *m* phase leads to an appreciable volume expansion, on the order of 4%. Therefore, the volume per molecule increases in the order from *t*- to *c*- to *m*-ZrO_2 for the prepared samples.

All specimens were cut into 10.59-mm disks, mechanically polished to a 1-μm diamond finish, and chemically polished with a colloidal-silica suspension[22] for a sufficient time to remove 25 μm of material. The last step is necessary to assure removal of the polishing damage layer and its associated high dislocation density. Polishing damage has been shown to affect the band gap of Al_2O_3 and MgO.[23] Samples were cleaned with trichloroethylene, acetone, and methanol prior to measurement.

B. VUV spectroscopy

Optical spectroscopy results for large band-gap materials like zirconia are not readily available because ultraviolet (UV) and visible reflectance measurements are limited to energies below 6 eV due to the absorption of air.[24] Presently there are no reported optical constants for ZrO_2 above 6 eV. For a comprehensive electronic structure study, VUV light sources such as the synchrotron or the laser plasma light source (LPLS) (Ref. 25) are required to encompass the valence-to-conduction band transitions of the intrinsic electronic structure.[26,27]

TABLE I. Structural parameters of ZrO_2 samples studied experimentally.

	c-ZrO_2- 9.5 mol % Y_2O_3	*t*-ZrO_2- 4.5 mol % Y_2O_3	*m*-ZrO_2
Form	Single crystal	Polycrystal	Extensively microtwinned single crystal
Lattice constant (Å)	$a=5.143$	$a=3.607$ $c=5.181$	
Volume/molecule (Å^3)	34.009	33.71	

Room-temperature reflectivity spectra were acquired at energies from 3 to 40 eV using a LPLS spectrophotometer. A complete description of the spectrophotometer has been published.[28] For the transparent single crystal c-ZrO_2 we used a Newton-Raphson method for two simultaneous equations[29] to calculate the single surface reflectance and absorption coefficient (α), using the measured total reflectance and the transmission of the sample, thereby compensating for the back surface reflectance that arises in transparent samples.[30,31] The index of refraction n was determined using a laser ellipsometer[32] with measurements made at 488 and 633 nm at angles of 50° and 70°. The reflectance data are scaled to match the refractive index in the visible region, and the optical properties calculated using Kramers-Kronig (KK) analysis.[33] In addition, the oscillator strength f-sum rule[34] is calculated to determine the valence-electron count.

Band-gap energies were determined for all three phases using the absorption coefficient (α) determined from KK analysis of the reflectance. Traditionally, band-gap energies are determined from experimental data using optical transmission measurements, but this was not possible for the t or m samples due to their opacity. Absorption coefficients determined from reflectance data span a very large dynamic range (typically 100 to 1×10^6 cm^{-1}) and most effectively probe high values of the absorption. Therefore, the band-gap energies reported here will typically be larger than those determined from transmission-based measurements. For a basis of comparison between theory and experiment, the theoretically determined optical properties were fitted in a similar manner as the experimental data. Band-gap energies were determined, assuming a direct gap model, by linear fitting to the steepest portion of a plot of α^2E^2, where E is energy.

C. Valence-band x-ray-photoemission spectroscopy

To determine the valence band (VB) density of states, VB-XPS spectra[35,36] were taken using monochromatized Al $K\alpha$ radiation. Small spot optics (300 μm) and a charge-neutralization flood gun were used to avoid charging effects. The resolution of the measurements was 0.7 eV (Au $4f_{7/2}$ linewidth). The samples studied were small (1.2 mm×1.2 mm×14 mm) bar samples, and the m and c samples were fractured *in situ* in ultrahigh vacuum to avoid contamination while the polycrystalline t sample was fractured in air prior to the measurement.

D. Band-structure and optical properties calculations

The orthogonalized linear-combination-of-atomic-orbitals (OLCAO) method has been successfully applied to the study of the electronic structure and optical properties of a variety of oxides.[37–50] The OLCAO band structures of the three phases of ZrO_2 were originally calculated whereby only the c phase was done self-consistently and the potential functions obtained for O and Zr were then used to calculate the band structure of the more complicated t and the m phases.[51] We have since recalculated the band structure self-consistently for all the three phases, using these wave functions for the calculation of the optical properties. The band-structure calculations were performed for idealized room-temperature crystal structures of the three phases of ZrO_2, and there was no Y_2O_3 stabilizer or oxygen vacancies incorporated in the structures used for the calculations. The structural parameters used in the band-structure calculations are summarized in Table II including unit-cell parameters, volumes per molecule, and Zr-O bond lengths. Since the percentage of stabilizer used in stabilized ZrO_2 samples strongly affects the structural parameters, there are noticeable differences between the samples studied and the structures calculated. For the crystal structures used in the band-structure calculations, the volume per molecule increases in the order from c- to t- to m-ZrO_2. The molecular volumes of the experimental samples and the crystal structures used for the calculations are comparable for the t and m phases, but there is a substantial difference between the experimental cubic sample and the theoretical cubic-crystal structure.

The details of the theoretical calculation have been amply described in the literature, so we only briefly outline the computational procedures of our calculations. In all three phases, we have used a basis function that consists of all the core orbitals plus the Zr $5s,4d,6s,6p,5d$ and O $2s,2p,3s,3p$ atomic orbitals. An orthogonalization to the core process was applied which reduces the sizes of the secular equations. The crystal potential is constructed according to the local-density approximation (LDA) with correction for the correlation effect using the Wigner interpolation formula, and is fitted to a set of atom-centered Gaussian functionals. We have attained an accuracy in the range of 0.000 005 to 0.000 01 electron per valence electron in the unconstrained charge-density fit in the self-consistent iteration procedure, which is generally adequate for band-structure studies. The energy eigenvalues and the wave functions are obtained at the 89, 140, 125 k points in the irreducible portion of the Brillouin zone of the c-, the t-, and the m-ZrO_2 cell, respectively.

The density of states (DOS) and the optical conductivity ($\sigma_1=i\omega\epsilon_2/4\pi$, where ω is the frequency and ϵ_2 is the imaginary part of the dielectric constant) curves were calculated using the linear analytic tetrahedron method.[52,53]

TABLE II. Structural parameters of ZrO_2 phases used in the OLCAO calculation.

	c-ZrO_2	t-ZrO_2	m-ZrO_2
Lattice constant (Å)	$a=5.086$	$a=3.606$ $c=5.180$	$a=5.151$ $b=5.212$ $c=5.317$ $\beta=99.23°$
Volume/molecule (Å^3)	32.887	33.665	35.22
Space group	$Fm3m$	$P42/nmc$	$P21/c$
Zr-O bond length (Å)	2.202	2.102(6) 2.351(7)	2.052(2) 2.063(2) 2.153(2) 2.157(2)

All the momentum matrix elements for dipole transitions between the occupied VB and the empty conduction band (CB) are evaluated exactly and included in the calculation. The real part of the dielectric constant (ϵ_1) is then determined from the Kramers-Kronig analysis of the imaginary part of the dielectric constant (ϵ_2), and the complex dielectric constant is used to calculate the optical-absorption coefficient α and the bulk energy-loss function.

III. RESULTS

A. VUV spectroscopy

The refractive indices for t-ZrO_2 at wavelengths of 488.0 nm (2.54 eV) and 632.8 nm (1.96 eV) were 2.208 ($n^2=\epsilon_1=4.875$) and 2.192 ($n^2=\epsilon_1=4.805$), respectively. A refractive index of approximately 2.16 ($n^2=4.606$) was found in the literature for c-ZrO_2.[54]

The reflectivities of m-, t-, and c-ZrO_2 from 3.5 to 40 eV are shown in Fig. 1. The highest reflectivity is found for the c-ZrO_2 sample. All three samples show a strong feature centered around ~8-eV, and two smaller features at ~22 and ~33.5 eV, respectively. In addition, the ~8-eV, feature shows evidence of a lower-energy shoulder or peak which varies among the three phases. The direct band gaps, found by extrapolation of the absorption coefficient curves are shown in Table III. The band-gap fits have been performed in two different ranges of the absorption coefficients to characterize the differences in the fundamental absorption edge of the three phases of ZrO_2. In the lower absorption coefficient range ($2.5\times10^5<\alpha<7\times10^5$), t- and m-ZrO_2 have comparable band-gap energies while c-ZrO_2 has a larger band-gap energy. In the higher absorption coefficient range ($7\times10^5<\alpha<1.5\times10^6$) t-ZrO_2 is still the lowest band-gap energy while c- and m-ZrO_2 have comparable band-gap energies. These differences in fitted band-gap energies arise from the strong low-energy shoulder which is seen in the optical conductivity in the region of the fundamental absorption edge. The higher α fitting range corresponds to band-gap energies determined at higher energy than this shoulder in the absorption edge.

TABLE III. Direct band-gap energy (eV) of ZrO_2 determined from experimental and theoretical data.

Fitting range (cm^{-1})	Cubic Expt.	Cubic Theor.	Tetragonal Expt.	Tetragonal Theor.	Monoclinic Expt.	Monoclinic Theor.
OLCAO B.S. $2.5\times10^5<\alpha<7\times10^5$ fit		4.93		4.28		4.46
Experiment $2.5\times10^5<\alpha<7\times10^5$ fit	6.1		5.78		5.83	
Experiment $7\times10^5<\alpha<1.5\times10^6$ fit	7.08		6.62		7.09	

The optical conductivity (σ_1) is shown in Fig. 2 and the measured transition energies are summarized in Table IV. The structure in the optical conductivity spectra is similar for the three zirconia phases. All three phases show their largest peak, referred to as E_1, located at ~8 eV. On the low-energy side of the E_1 peak, there is evidence of a shoulder (E_1') at ~6.5 eV, which is most prominent in the m phase and is least dramatic in the c phase. The c phase is characterized by a very rapid increase in σ_1 from the band gap to E_1. The c and t materials show similar behavior on the high-energy side of E_1, while the m phase exhibits a plateau of transitions that extends from E_1 to E_1''. At ~16.7 eV there is a small shoulder (E_2) present in the c and t materials that appears to increase with the mol% Y_2O_3. The next prominent feature in the spectra for all three materials is

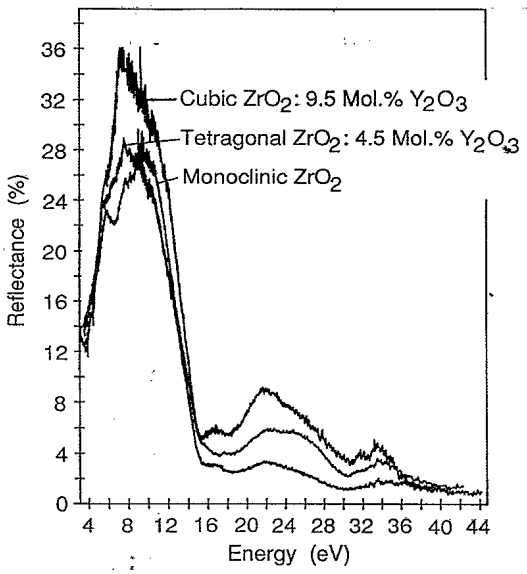

FIG. 1. Room-temperature reflectivities of cubic (9.5 mol % Y_2O_3), tetragonal (4.5 mol % Y_2O_3), and monoclinic zirconia.

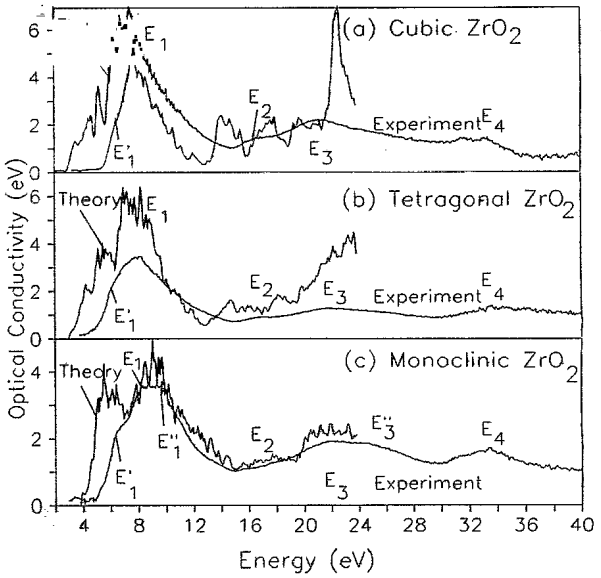

FIG. 2. Measured and calculated optical conductivities ($\sigma_1=i\omega\epsilon_2/4\pi$) of (a) cubic, (b) tetragonal, and (c) m-ZrO_2.

a broad peak (E_3) at ~21.5 eV. This peak is located at the same energy for all three materials. The m phase again is characterized by a plateau of transitions from E_3 to E_3'' at 24.5 eV. The final structure in the three spectra is the E_4 peak at ~33.5 eV.

B. Valence-band XPS

The VB x-ray-photoemission spectra for the three phases of ZrO_2 are shown in Fig. 3, and the results summarized in Table V where the energies are referenced to the VB maximum. The upper VB varies from O 2p nonbonding and O-cation hybridized bonding orbitals and extends from 0 to −7 eV binding energy, and is not seen to vary among the three phases of ZrO_2. The O 2s band is broad and appears at −19 eV, while the Zr 4p band is seen as a doublet at −28 eV. Two other important features are seen in the VB region. First, at −14.5 eV there is a peak that arises from occupied Zr 4d states which can be associated with Zr^{2+} ions. In a ZrO_2 molecule, the formal oxidation state of Zr is 4+, with the result that the Zr 4d orbitals are completely unoccupied and give rise to the Zr 4d CB's. But in these stabilized samples of ZrO_2 there is some reduction of the Zr oxidation state which leads to the appearance of occupied Zr 4d states in the VB region. Second, the stabilizing dopant used in the t- and c-ZrO_2 samples, Y, gives rise to a VB of Y 4p states at −23 eV. The Y 4p peak in these samples increases in intensity as the mol % Y_2O_3 increases.

C. Theoretical

The self-consistent band structures of the three phases of ZrO_2 along the lines of high symmetry are shown in Figs. 4–6. In addition, the electron binding energies determined from the DOS previously reported by Zandiehnadem, Murray, and Ching, are summarized in Table V. The theoretical O 2p width is 6 eV and is similar for all three phases. The next lower VB arises from O 2s and appears at −17 to −16 eV depending on the phase. The Zr 4p states are not seen in the band structure because they are treated as core states and thus eliminated from the orthogonalization procedure. The occupied Zr 4d states that arise in the samples from Zr^{2+} are also not present in the calculated structures. Also, the Y 4p states are absent in the calculated DOS since Y defects are not included in the calculation. The low-lying CB's of ZrO_2 arise from unoccupied Zr 4d states, and exhibit large changes as the symmetry of the crystal structure is reduced from c to m. In c-ZrO_2 the Zr 4d bands are well split into a lower-energy d band arising from the x^2-y^2 and z^2 orbitals while a higher energy band arises from the

TABLE IV. Transition energies (eV) in ZrO_2 determined from experimental and theoretical data.

Transition	Origins	Cubic		Tetragonal		Monoclinic	
		Expt.	Theor.	Expt.	Theor.	Expt.	Theor.
E_1'	O 2p(VB)→ Zr 4d(CB)	6.5	5.2	6.0	5.2	6.5	5.1
E_1	O 2p(VB)→ Zr 4d(CB)	7.9	7.3	8.0	7.8	8.2	8.3
E_1''	O 2p(VB)→ Zr 4d(CB)	a	a	a	a	9.8	9.7
E_2	O 2p(VB)→ Y(CB)	16.7	a	16.8	a	a	a
E_3	O 2p(VB)→ Zr 5s(CB) or O 2s(VB) to Zr 4d(CB)	21.1	22.5	21.7	~24	21.8	22
E_3''	O 2p(VB)→ Zr 5s(CB) or O 2s(VB) to Zr 4d(CB)	a	a	a	a	24.5	a
E_4	O 2s(VB)→ Zr 4d(CB) or Zr 4p(VB)→ Zr 4d(CB)	33	a	34	a	33.3	a

[a]Not applicable.

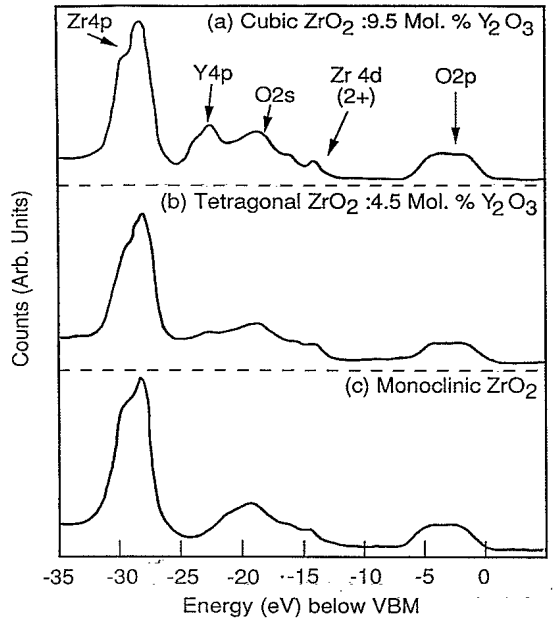

FIG. 3. Valence-band XPS of (a) cubic, (b) tetragonal, and (c) monoclinic zirconia.

xy, *yz*, and *zx* type *d* orbitals. In *t*-ZrO_2 the separation between these *d* orbital bands almost disappears, but the presence of two discrete bands is still evident in the DOS. In the very-low-symmetry *m* case, the *d* orbitals are degenerate and the CB has a very different structure, appearing as a single band in the DOS.

The calculated conductivity functions for a photon energy of up to 40 eV for the three phases of ZrO_2 are shown in Fig. 2 compared to the measured spectra and the transition energies listed in Table IV. It is obvious that the gross features of the measured data are reproduced by the calculation. Specifically, we note that (1) all three phases have the major absorption between 4 and 12 eV. The *c* phase has the highest intensity E_1 peak in this range and the *m* and the *t* phases have comparable intensities. (2) Both the *t* and the *m* phases have a prominent shoulderlike structure (E_1') on the low-energy side of the E_1 peak. This feature is also reproduced by the calculation as additional peak structures in that region. (3) The *m* phase exhibits a broad plateau of transitions extending from E_1 to E_1''. (4) All three phases studied experimentally have an absorption minimum at ~ 15 eV, while the calculations show minima at 13 eV for the *c* and *t* phases and at 15 eV for the *m* phase. (4) Beyond 15 eV, the absorption for all three phases starts to increase at the E_3 peak, which appears experimentally at 21–22 eV. The calculated σ_1 also shows a rise to form the E_3 peak in this region. The calculations show the same features qualitatively.

IV. DISCUSSION

A. Limitations of the study

Due to the fundamental complexity of dopant-induced phase stabilization of ZrO_2, it is not possible at present to undertake experimental and theoretical studies of identical systems. A room-temperature study of the three phases required using dopant-stabilized *t*- and *c*-ZrO_2. These materials have substantial dopant concentrations, and also have high concentrations of dopant-induced oxygen vacancies. The stabilizers strongly affect the unit-cell volumes of the *t* and *c* phases, leading to larger unit-

TABLE V. Valence- and conduction-band binding energies (eV) in ZrO_2 determined from experimental and theoretical data. [Theoretical DOS results from Zandiehnadem and Murray (Ref. 4).]

Transition	Cubic		Tetragonal		Monoclinic	
	Expt.	Theor.	Expt.	Theor.	Expt.	Theor.
Zr 4*d* (*xy*,*yz*,*zx*)	a	8 center 7–10	a	8.5 center 7–10	a	Zr 4*d* combined
Zr 4*d* (x^2-y^2,z^2)	a	4.5 3.8–5.5	a	5.3 4.1–7	a	7 center 4.5–10
Energy gap						
O 2*p*	0 to −7	0 to −7		0 to −6	0 to −7	0 to −5
Zr 4*d* (2^+)	−14.5 center	a		a	−14.5 center	a
O 2*s*	−19 center −16 to −24	−17		−16.5	−19 center −16 to −24	−16
Y 4*p*	−23 center	a		a	a	a
Zr 4*p*	−28 center −26 to −33	a		a	−28 center −26 to −33	a

[a]Not observed.

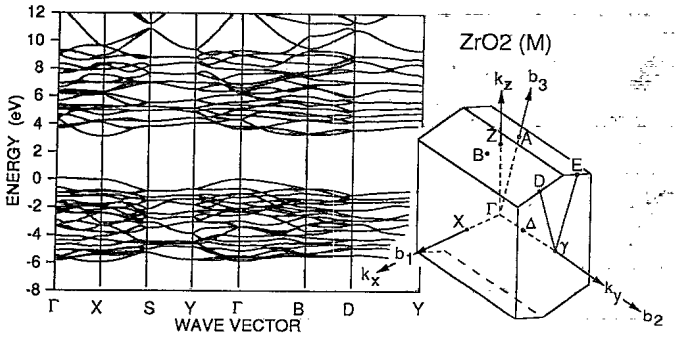

FIG. 4. OLCAO band structure of monoclinic zirconia.

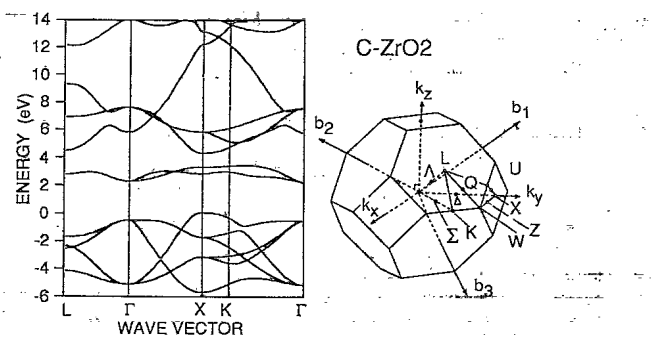

FIG. 6. OLCAO band structure of cubic zirconia.

cell volumes than the idealized structures. In addition, single-crystal samples would be optimal for this study, but no source of suitable t-ZrO_2 is available due to its metastability, while the melt-grown sample of m-ZrO_2 is highly microtwinned and strained. Therefore, the experimental samples are affected by the presence of the stabilizing dopants and defects and their crystalline form. By comparison the band-structure calculations are performed for idealized room-temperature dopant-free structures, which for the c and t phases are unstable. One consequence of this appears in the results for stabilized c-ZrO_2 where the effective Zr coordination in the sample is sevenfold, as is found in the m structure, while the band structure is for fully eightfold coordinated Zr. The necessary role of stabilizers and vacancies in producing stabilized room-temperature structures is at this time ignored. Therefore, these two phenomena, the role of the stabilizers in the experimental data and the idealized structures used for the band-structure calculations, must be kept in mind in the discussion. Even considering the limitations of this initial attempt at understanding the electronic structure of three phases of ZrO_2, considerable insight can be gained.

The acceptable agreement between the experimental and theoretical results is shown in the comparison of the optical conductivities shown in Fig. 2. In addition, the oscillator strength or f-sum rule is plotted in Fig. 7. The sum rule plateaus at 12 electrons per ZrO_2 molecule, where the valence electron count for ZrO_2 would be 16 [2 O$=2^*(2s^22p^4)=12$, Zr$=4d^25s^2=4$, sum$=16$]. Therefore, within the approximation of the effective mass, the valence electrons are reasonably tallied for the three phases. The theoretical results show the sum rule increasing at lower energy due to the LDA underestimation of the band-gap energy, and all three phases show shapes comparable to the experimental results.

To determine the crystal-structure-induced changes in the electronic structure of ZrO_2 comparable changes must be seen in our theoretical and experimental results. Changes which only appear in the experimental results may arise from the stabilizing dopants and defects.

B. Valence bands

The VB's of the three phases are very similar. The stabilizing dopants and defects give rise to the appearance of Y 4p states in the VB's, and also the appearance of Zr 4d states associated with stabilization-induced reduction of the effective ionization state of Zr^{4+} towards Zr^{2+}. These findings are not seen in the idealized structures because they are associated with the effective sevenfold coordination of Zr by O, and this reduction of Zr may play a strong role in the phase stabilization.

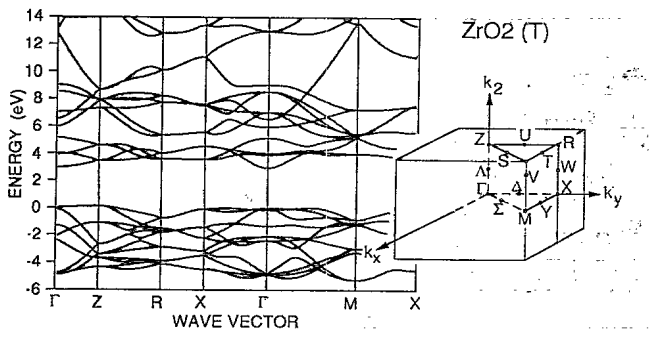

FIG. 5. OLCAO band structure of tetragonal zirconia.

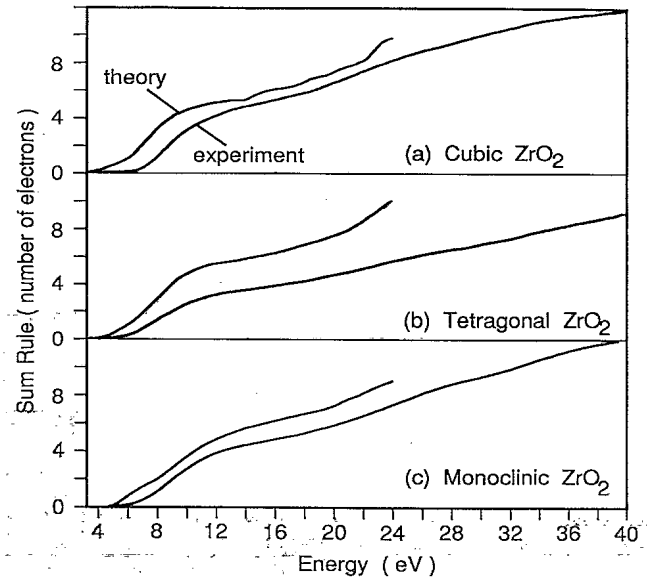

FIG. 7. Oscillator strength f-sum rule for the measured and calculated optical properties of (a) cubic, (b) tetragonal, and (c) monoclinic ZrO_2.

C. Interband transitions

The interband transitions seen in the experimental optical conductivity results (Fig. 2) and the calculated values summarized in Table IV are very similar, demonstrating the high quality of the band-structure-derived optical properties reported here. For all three phases the theoretical calculation underestimates the band-gap energy as expected under the LDA. In general the largest band-gap energy is seen for the c-ZrO_2 phase. The E_1 peak is the largest feature in the optical properties and arises due to transitions from the O $2p$ VB to the Zr $4d(x^2\text{-}y^2,z^2)$ CB. The width of the complete E_1 peak is dictated by the O $2p$ VB width. The changes in the E_1 peak are associated with the growth of the E_1' shoulder progressing to the m phase and the appearance of the E_1'' transitions in the m phase. These changes arise from the crystal structure change from c to m and the resulting lowering of the symmetry with the associated folding in of the Brillouin zone. As is seen in the calculated conduction bands, the crystal-structure change breaks the degeneracy of the two d orbital bands broadening and mixing them leading to a transformation of the lowest two Zr CB's.

The E_2 transition scales with Y content and is not seen in the theoretical results. The prominent Y $4p$ VB is at too large of a binding energy (-23 eV) to be involved in this 16.7-eV transition. Therefore, the E_2 transition must arise from O $2p$ VB to Y CB transitions. In lanthanum stabilized Y_2O_3 a similar transition is seen at 17 eV.[55]

The E_3 transitions seen in both the theoretical and experimental results have two possible origins. These transitions appear over a wide energy range ($\sim$18–28 eV) and may arise from transitions between the O $2p$ VB and the Zr $5s$ CB which lies at 10–15 eV above the VB. This Zr $5s$ CB is the third major CB, lying above the Zr $4d$ $(x^2\text{-}y^2,z^2)$ and the Zr $4d$ (xy,yz,zx). The other possibility is that the E_3 transitions correspond to excitations from the broad O $2s$ VB to the Zr $4d$ CB. From this point of view, the appearance in the m phase of the E_3'' transitions at an energy above the E_3 energy mirrors the same phenomena as seen in the E_1 peak due to the large changes in the Zr $4d$ CB's.

The E_4 transitions, therefore, arise from the next VB below O $2s$, consisting of transitions from the Zr $4p$ VB to the Zr $4d$ conduction bands.

D. Effects of crystal structure

Crystal structure plays a strong role in the electronic structure of ZrO_2. This effect is most apparent in the d-electron-derived CB's. The distortion associated with the transformation from c to t is relatively small and the CB's change slightly. In this case the most dramatic change is the reduction of the CB gap between the Zr $4d$ $(x^2\text{-}y^2,z^2)$ and the Zr $4d$ (xy,yz,zx) CB's which is present in c-ZrO_2 and disappears in t-ZrO as can be seen in Figs. 5 and 6. The phase transformation from t to m is much more dramatic, with a substantial volume expansion, and the Zr $4d$ CB's are hybridized into a new single Zr $4d$ CB.

The crystal-structure changes are readily apparent in the theoretical results and prominently change the experimentally determined transitions of the E_1 peak. Still, in the dopant-stabilized samples the structural changes associated with c, t, and m phases may be less dramatic since the role of the stabilizers in the c and t phases is to structurally imitate the local structural characteristics of the m phase.

The stabilizing dopant used, in this case Y, also affects the electronic structure of real ZrO_2 materials. For example, Y will introduce $4d$-electron-derived CB's and $4p$-electron-derived VB's. Still, the appearance of the d-electron CB's cannot play an important role in the stabilization since Mg and Ca, neither of which bear d electrons, also efficiently stabilize the ZrO_2 phases.

A more important role of the stabilizers in the electronic structure, which we have not emphasized here, may arise from the indirect role of the dopant-induced oxygen vacancies. These oxygen vacancies are present in stabilized materials at high concentrations, for example, 9.5 mol % Y_2O_3 stabilized c-ZrO_3 contains 4.75% oxygen vacancies. These oxygen vacancies are situated adjacent to Zr atoms and reduce the symmetry and coordination of the Zr site. This coordination-based mechanism may be similar to the crystal-structure-induced Zr $4d$ hybridization seen in the m band structure calculated here. In addition, the oxygen vacancies present at high concentration can introduce defect bands in the valence-band and conduction-band regions which also strongly affect the electronic structure.[56]

Given the fact that the calculations are for perfect crystals, while the measurements are on samples containing many defects and imperfections, the above agreements, even though qualitative in nature, are better than expected, and indicate that the theoretical band structures for the three phases of zirconia are basically correct. The major discrepancies are as follows.

(1) The absorption edges in the calculated spectra are smaller than those measured by about 1 eV. This is related to the fact that the local-density approximation in the electronic-structure calculations generally underestimates the band gap.

(2) The theoretical calculations show a greater variation among the three phases than the experimental data suggest.

(3) For the c phase, the calculation shows additional structure above 12 eV which is not at all obvious in the experimental curve. However, as mentioned before, the perfect c phase used in the calculation is only a hypothetical structure.

It will be desirable to include in the calculation the specific lattice defects such as the associated Y impurity and O vacancy to see if the agreements between the theory and the experiment can be improved.

V. CONCLUSIONS

The electronic structure of three phases of ZrO_2 has been determined experimentally and theoretically. The experimental samples studied contain perforce, stabilizing dopants, and defects, while the band-structure calculations have been performed for idealized room-

temperature structures, neglecting the presence of stabilizing dopants or defects. Even considering the limitations of this initial attempt at obtaining the electronic structure of three phases of ZrO_2, considerable insight can be gained. The predominant interband transitions are the O $2p$ to Zr $4d$ at ~ 8 eV (E_1), O $2s$ to Zr $4d$ at ~ 22 eV (E_3), and Zr $4p$ to Zr $4d$ transitions at ~ 34 eV (E_4). As the symmetry of the ZrO_2 is reduced from cubic to monoclinic, the gap between Zr $4d$ (x^2-y^2 and z^2) and the Zr $4d$ (xy, yz, and zx) bands decreases and disappears, producing an evolution of the E_1 and E_3 peak structures.

In the stabilized materials, the effective reduction of the zirconium coordination by oxygen from eightfold to sevenfold leads to the introduction of occupied Zr $4d$ valence bands which are associated with Zr^{2+}. These results are not observed in the idealized structures, and this reduction of Zr may play a strong role in the phase stabilization. In addition, transitions are seen at ~ 17 eV which scale with yttrium content and arise from O $2p$ to Y $4d$ transitions, while an independent valence band of Y $4p$ character is introduced with increasing dopant concentration.

ACKNOWLEDGMENTS

The authors would like to acknowledge the assistance of D. J. Jones with the VUV spectroscopy, J. F. Wenckus of Ceres Corporation for supplying the cubic and monoclinic ZrO_2 samples, L. F. Lardear, R. L. Harlow, and C. M. Foris for assistance with x-ray diffraction, and K. G. Lloyd for the XPS of t-ZrO_2. The work at the University of Missouri–Kansas City was supported by the U.S. Department of Energy Grant No. DE-FG02-84ER45170.

*Present address: Dept. 1845, Sandia National Laboratories, Albuquerque, NM 87185-0607.

†Present address: Dept. of Materials Science & Engineering, FB-10, University of Washington, Seattle, WA 98195.

[1]M. Yoshimura, Ceram. Bull. **67**, 1950 (1988).

[2]C. K. Kwok and C. R. Aita, J. Appl. Phys. **66**, 6 (1989); **66**, 2756 (1989).

[3]D. W. Liu, C. H. Perry, and R. P. Ingel, J. Appl. Phys. **64**, 3 (1988); **64**, 1413 (1988)

[4]F. Zandiehnadem, R. A. Murray, and W. Y. Ching, Physica B **150**, 19 (1988).

[5]W. Y. Ching, D. E. Ellis, and D. J. Lam, in *Materials for Infrared Detectors and Sources,* edited by R. F. C. Farrow and J. F. Schetzing, MRS Symposia Proceeding No. 90 (Materials Research Society, Pittsburgh, 1987), p. 181.

[6]R. Kikuchi and B. P. Burton, Physica B **150**, 132 (1988).

[7]M. Morinaga, H. Adachi, and M. Tsukada, J. Phys. Chem. Solids **44**, 301 (1983).

[8]R. H. French, D. E. Ellis, F. S. Ohuchi, V. C. Long, W. Y. Ching, and D. J. Lam (unpublished).

[9]H. J. F. Jansen and J. A. Gardner, Physica B **150**, 10 (1988).

[10]A. H. Heuer, J. Am. Ceram. Soc. **70**, 689 (1987).

[11]R. McMeeking and A. G. Evans, J. Am. Ceram. Soc. **65**, 242 (1982).

[12]D. Yuan and F. A. Kroger, J. Electrochem. Soc. **116**, 594 (1969).

[13]C. B. Alcock, Mater. Sci. Res. **10**, 419 (1975).

[14]H. S. Isaacs, in *Science and Technology of Zirconia,* Advances in Ceramics Vol. 3, edited by A. H. Heuer and L. W. Hobbs (American Ceramic Society, Columbus, OH, 1981), pp. 406–418.

[15]F. Zandiehnadem, R. A. Murray, and W. Y. Ching, Physica B **150**, 19 (1988).

[16]For example, see W. Y. Ching, D. E. Ellis, and D. J. Lam, in *Materials for Infrared Detectors and Sources* (Ref. 5).

[17]Ceres Corporation, North Billerica, MA 01862.

[18]K. Nassau, Lapidary J. **35**, 1194 (1981); **35**, 120 (1981).

[19]TZ-3YA Zirconia, Tosoh USA Inc., Bridgewater, New Jersey.

[20]S. J. Glass and D. J. Green, in *Ceramic Transactions 1b, Ceramic Powder Science,* edited by G. L. Messing, E. R. Fuller, and H. Hausner (The American Ceramic Society, Westerville, Ohio, 1988), pp. 784–791.

[21]R. P. Ingel and D. Lewis III, J. Am. Ceram. Soc. **69**, 4 (1986); **69**, 325 (1986).

[22]Struers, Inc., Westlake, Ohio.

[23]H. Song, R. H. French, and R. L. Coble, J. Am. Ceram. Soc. **72**, 990 (1989).

[24]R. H. French, in *Advanced Characterization Techniques for Ceramics,* in Ceramic Transactions Vol. 5, edited by W. S. Young, G. L. McKay, and G. E. Pike (American Ceramic Society, Westerville, OH, 1989), pp. 406–414.

[25]M. L. Bortz and R. H. French, Appl. Phys. Lett. **55**, 1955 (1989).

[26]R. H. French, J. Am. Ceram. Soc. **73**, 477 (1990); R. H. French, D. J. Jones, and S. Loughin, J. Am. Ceram. Soc. **77**, 2 (1994).

[27]M. L. Bortz, R. H. French, D. J. Jones, R. V. Kasowski, and F. S. Ohuchi, Phys. Scr. **41**, 537 (1990); S. Loughin, R. H. French, W. Y. Ching, Y. N. Xu, and G. A. Slack, Appl. Phys. Lett. **63**, 1182 (1993).

[28]R. H. French, Phys. Scr. **41**, 404 (1990).

[29]See, for example, W. H. Press, B. P. Flannery, S. A. Teukolsky, and W. T. Vetterling, *Numerical Recipes—The Art of Scientific Computing* (Cambridge University Press, Cambridge, 1986), p. 269.

[30]M. E. Innocenzi, R. T. Swimm, M. Bass, R. H. French, A. B. Villaverde, and M. R. Kokta, J. Appl. Phys. **67**, 12 (1990); **67**, 7542 (1990).

[31]M. E. Innocenzi, R. T. Swimm, M. Bass, R. H. French, and M. R. Kokta, J. Appl. Phys. **68**, 3 (1990); **68**, 1200 (1990).

[32]Gaertner Scientific Corporation, Chicago, Illinois.

[33]M. L. Bortz and R. H. French, Appl. Spectrosc. **43**, 1498 (1989).

[34]D. Y. Smith, in *Handbook of Optical Constants of Solids,* edited by E. D. Palik (Academic, New York, 1985), pp. 35–68.

[35]G. Margaritondo and J. H. Weaver, in *Methods of Experimental Physics,* edited by R. L. Park and M. G. Lagally (Academic, New York, 1985), Vol. 22, pp. 127–185.

[36]F. S. Ohuchi and M. Kohyama, J. Am. Ceram. Soc. **74**, 6 (1991); **74**, 1163 (1991).

[37]W. Y. Ching, J. Am. Ceram. Soc. **73**, 11 (1990); **73**, 3135 (1990).

[38]G. -L. Zhao, Y. -N. Xu, W. Y. Ching, and K. W. Wong, Phys. Rev. B **36**, 7203 (1987).

[39]W. Y. Ching, G. -L. Zhao, Y. -N. Xu, and K. W. Wong, Mod. Phys. Lett. B **3**, 263 (1989).

[40]G. -L. Zhao, W. Y. Ching, and K. W. Wong, J. Opt. Soc. Am. B **6**, 505 (1989).
[41]W. Y. Ching, Y. -N. Xu, and K. W. Wong, Phys. Rev. B **40**, 7684 (1989).
[42]Y. -N. Xu and W. Y. Ching, Phys. Rev. B **41**, 5471 (1990).
[43]Y. N. Xu, W. Y. Ching, and R. H. French, Ferroelectrics **111**, 23 (1990).
[44]J. C. Parker, D. J. Lam, Y. -N. Xu, and W. Y. Ching, Phys. Rev. B **42**, 5289 (1990).
[45]W. Y. Ching and Y. -N. Xu, Phys. Rev. Lett. **65**, 895 (1990).
[46]J. C. Parker, D. J. Lam, Y. -N. Xu, and W. Y. Ching, Phys. Rev. B **42**, 4460 (1990).
[47]J. C. Parker, U. W. Gelser, D. J. Lam, Y. -N. Xu, and W. Y. Ching, J. Am. Ceram. Soc. **71**, 3206 (1990).
[48]Y. -N. Xu and W. Y. Ching, Phys. Rev. B **43**, 4463 (1991).
[49]W. Y. Ching, and Y. -N. Xu, Phys. Rev. B **44**, 5332 (1991).
[50]Y. -N. Xu and W. Y. Ching (unpublished).
[51]F. Zandiehadem, R. A. Murray, and W. Y. Ching, Physica B **150**, 19 (1988).
[52]G. Lehmann and M. Taut, Phys. Status Solidi B **54**, 469 (1972).
[53]G. Gilat and N. R. Bharatiya, Phys. Rev. B **12**, 8 (1975); **12**, 3479 (1975).
[54]D. L. Wood and K. Nassau, Appl. Opt. **12**, 2978 (1982).
[55]R. H. French, D. J. Jones, and G. Wei (unpublished).
[56]R. H. French, M. K. Crawford, R. D. Shannon, and M. L. Bortz (unpublished).